Journal of Computational Physics **159,** 172–196 (2000)
doi:10.1006/jcph.2000.6426, available online at http://www.idealibrary.com on IDEAL®

Large-Wave Simulation (LWS) of Free-Surface Flows Developing Weak Spilling Breaking Waves

Athanassios A. Dimas* and Laurie T. Fialkowski†

**Department of Mechanical Engineering, University of Maryland, College Park, Maryland 20742;*
†*Acoustic Systems Branch, Naval Research Laboratory, Washington, DC 20375*
E-mail: *adimas@eng.umd.edu and †lfialkowski@milton.nrl.navy.mil

Received March 31, 1999; revised September 17, 1999

A methodology, called large-wave simulation (LWS), is presented for the numerical simulation of free-surface flows past the appearance of spilling breakers. LWS is designed to resolve only the large, energy-carrying scales of the flow and model the effect of the subgrid, small-wavelength scales of the flow spectrum. This part of the spectrum includes the characteristic frothy whitecaps associated with spilling breakers. Modeling in LWS is based on the consistent application of spatial filtering on both the velocity field and the free-surface elevation. The subgrid scale (SGS) effect is modeled by two sets of stresses: (i) the eddy SGS stresses, which are identical to the ones arising in large-eddy-simulation of flows without a free surface, and (ii) the wave SGS stresses, which incorporate the free-surface effect. Both SGS stresses are modeled by eddy-viscosity models with constant coefficients. The methodology is applied on two free-surface flows: (i) the interaction of a plane gravity wave with a surface wake layer, and (ii) the nonlinear evolution of a surface shear layer instability. A priori and a posteriori tests show good agreement between the proposed model and actual SGS stresses, while LWS of both flows successfully continue past the breaking point as opposed to corresponding direct numerical simulations. For the first flow, LWS predicts the postbreaking appearance of a recirculating flow region in the wake of the breaker in qualitative agreement with experimental observations.

1. INTRODUCTION

In several problems, the evolution of free-surface flows leads to the development of steady or unsteady spilling breaking waves. Unsteady spilling breakers in the ocean are usually generated by wind or wave/wave interactions and play an important role in air/sea interactions because they influence momentum and energy transfer from the wave field to the underlying flow and are the major mechanism of wave energy dissipation [16]. Steady

0021-9991/00 $35.00

spilling breaking waves are usually found in the wave system of ships, where they convert kinetic and potential energy from the wave system into turbulent kinetic energy in the wakes of the breakers. These turbulent breaker wakes are momentum deficient, like the wake of a towed body [2, 7, 8]. Ship breakers are responsible for increased drag on ships [1] and play an important role in ship detection.

In all these problems, it is important to study the evolution of the wave field and the underlying turbulent flow past the breaking point. In terms of numerical simulations of free-surface flows, though, most present methodologies are unable to numerically predict the evolution of spilling breakers past the breaking point. The development of breaking waves is associated with a continuous slope increase of the free-surface elevation toward an infinite slope and overturning, which causes floating-point problems to numerical methods [5, 6] that require the resolution of all the free-surface flow scales during and after breaking. The most promising method, so far, has been the surface marker and micro-cell (SMMC) method by Chen *et al*. [3] that overcomes problems with free-surface overturnings but is also based on the requirement that all flow scales are resolved during and after a wave breaking event.

In this paper, a very different approach is presented that eliminates the need to resolve all scales for free-surface flows with spilling breakers. It has been observed in experiments [9] that, in the case of spilling breakers, the lengths and heights of the steep waves in the breaking region are very small compared to the spatially averaged free-surface elevation (Fig. 1). This last observation leads to the idea of performing large wave simulations (LWS) of spilling breakers past the breaking point, where only the large scales (velocity and free-surface elevation) of the flow are fully resolved while the effect of the small subgrid scales is modeled without resolving their shape. Therefore, the concept of a large wave simulation is based on the consistent and systematic introduction of the large-eddy-simulation (LES) methodology in free-surface flows. For free-surface flows, though, the physics of the problem is represented not only by the equations of motion but by the unknown shape of the free boundary as well. Therefore, use of filtering in the equations of motion only, as in LES, is not consistent with the presence of free-surface waves. The free surface has to participate in the filtering process.

A major advantage of LWS modeling of breaking is the naturally adaptive character of the model, since it is activated automatically by the dynamics of the resolved scales when breaking is about to occur. The close relationship between LWS modeling and LES modeling and the success of LES modeling in turbulent flows are positive indicators for the successful use of LWS in turbulent free-surface flows with spilling breakers. A detailed presentation of the methodology is given in the next two sections, followed by a description of the numerical method in Section 4. A priori tests of the proposed model are presented in Section 5, while a posteriori tests and results from two LWS of a free-surface flow past the breaking point are given in Section 6.

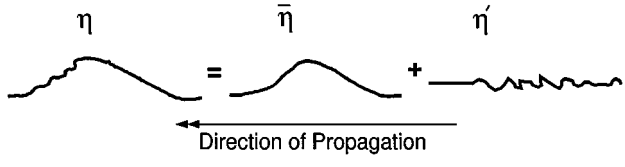

FIG. 1. Free-surface elevation decomposition for a typical spilling breaker. The lengths and heights of the subgrid scale waves at the breaking region are very small compared to the spatially filtered free-surface elevation $\bar{\eta}$.

2. LWS FORMULATION

The LWS formulation is based on the consistent application of a spatial filtering operation on all flow variables (velocities, pressure, free-surface elevation) in order to derive the equations of motion for the resolved scales. For any variable f, its resolved large-scale component $\bar{f}$ is obtained by

$$\bar{f}(\mathbf{x}, t) = \int_V f(\mathbf{r}, t)\, \bar{G}(\mathbf{x}, \mathbf{r}; \Delta)\, \mathrm{d}\mathbf{r}, \tag{1}$$

where $\mathbf{x}$ and $\mathbf{r}$ are position vectors, t is time, V is the flow domain, $\bar{G}$ is the filter function, and Δ is the size of the smallest resolvable scale. Filtering of the velocity field, for example, produces the following decomposition of the velocity components, $u_i,\ i = 1, 2, 3$,

$$u_i = \bar{u}_i + u_i', \tag{2}$$

where $\bar{u}_i$ corresponds to the resolved scale and u_i' corresponds to the unresolved subgrid scale. An equivalent decomposition is performed on the free-surface elevation, η, according to

$$\eta = \bar{\eta} + \eta', \tag{3}$$

where $\bar{\eta}$ corresponds to the resolved large-wavelength scale of the free-surface elevation and η' corresponds to the unresolved subgrid scale (Fig. 1). The free-surface elevation is a function of two spatial coordinates, therefore, a two-dimensional filtering operation equivalent to (1) is used.

For an incompressible, inviscid, free-surface flow, the equations of motion are the continuity equation

$$\frac{\partial u_i}{\partial x_i} = 0, \tag{4}$$

and the Euler equations

$$\frac{\partial u_i}{\partial t} + u_j \frac{\partial u_i}{\partial x_j} = -\frac{\partial p}{\partial x_i}, \tag{5}$$

where t is time, x_i are the cartesian coordinates ($x_1,\ x_3$ are the horizontal coordinates, x_2 is positive in the opposite direction of gravity, and $x_2 = 0$ corresponds to the undisturbed free-surface level), u_i is the velocity field, p is the dynamic pressure [$p = P - (-x_2/\mathrm{Fr}^2)$] defined as the difference between pressure, P, and hydrostatic pressure, and Fr is the Froude number of the flow. All variables have been rendered dimensionless by a characteristic flow velocity U_∞, and a characteristic length scale b; therefore, the dimensionless Froude number is defined as $\mathrm{Fr} = U_\infty/\sqrt{gb}$, where g is the gravity acceleration.

The dynamic and kinematic boundary conditions on the free surface ($x_2 = \eta(x_1,\ x_3,\ t)$), respectively, are

$$p = \frac{\eta}{\mathrm{Fr}^2} \tag{6}$$

$$u_2 = \frac{\mathrm{d}\eta}{\mathrm{d}t} = \frac{\partial \eta}{\partial t} + u_j \frac{\partial \eta}{\partial x_j}, \tag{7}$$

where d/dt is the material derivative operator. Surface tension effects are not considered in this study.

In the above formulation, the free-surface elevation is an unknown function of time, which renders the flow domain time-dependent and complicates the computation of the filtering integral in (1). To overcome this problem, boundary-fitted coordinates are introduced according to

$$x_1^* = x_1, \qquad x_2^* = x_2 - \eta(x_1, x_3, t), \qquad x_3^* = x_3, \qquad t^* = t, \tag{8}$$

where x_1^*, x_2^*, and x_3^* are the coordinates in the transformed domain. The above transformation is intended to be used only for flows with infinite depth ($x_2 \to -\infty$) without the presence of solid boundaries. Derivatives are transformed as follows:

$$\frac{\partial}{\partial x_1} = \frac{\partial}{\partial x_1^*} - \frac{\partial \eta}{\partial x_1^*}\frac{\partial}{\partial x_2^*}, \qquad \frac{\partial}{\partial x_2} = \frac{\partial}{\partial x_2^*}, \qquad \frac{\partial}{\partial x_3} = \frac{\partial}{\partial x_3^*} - \frac{\partial \eta}{\partial x_3^*}\frac{\partial}{\partial x_2^*},$$
$$\frac{\partial}{\partial t} = \frac{\partial}{\partial t^*} - \frac{\partial \eta}{\partial t^*}\frac{\partial}{\partial x_2^*}. \tag{9}$$

At this point, no transformation is attempted on the dependent variables (velocity and pressure) in order that they be filtered in their physical form.

Then, according to (8) and (9), the continuity and Euler equations, respectively, become

$$\frac{\partial u_i}{\partial x_i^*} - \frac{\partial u_1}{\partial x_2^*}\frac{\partial \eta}{\partial x_1^*} - \frac{\partial u_3}{\partial x_2^*}\frac{\partial \eta}{\partial x_3^*} = 0 \tag{10}$$

$$\frac{\partial u_i}{\partial t^*} + u_j\frac{\partial u_i}{\partial x_j^*} - H_i = -\frac{\partial p}{\partial x_i^*}, \tag{11}$$

where

$$H_i = u_1\frac{\partial u_i}{\partial x_2^*}\frac{\partial \eta}{\partial x_1^*} + u_3\frac{\partial u_i}{\partial x_2^*}\frac{\partial \eta}{\partial x_3^*} + \frac{\partial u_i}{\partial x_2^*}\frac{\partial \eta}{\partial t^*} + \frac{\partial p}{\partial x_2^*}\frac{\partial \eta}{\partial x_i^*}, \tag{12}$$

while the dynamic and kinematic free-surface boundary conditions, (6) and (7) respectively, become

$$p = \frac{\eta}{\mathrm{Fr}^2} \tag{13}$$

$$u_2 = \frac{\mathrm{d}\eta}{\mathrm{d}t^*} = \frac{\partial \eta}{\partial t^*} + u_j\frac{\partial \eta}{\partial x_j^*} \tag{14}$$

and are applied at $x_2^* = 0$. With this formulation, the transformed free-surface boundary, and hence the flow domain, are not functions of time, while the influence of the free-surface elevation on the physics of the flow introduces new terms in the transformed equations of motion.

The governing equations for the resolved scales are obtained by applying the filtering operation (1) to the transformed equations of motion. In this paper, two-dimensional flows (on the $x_1 - x_2$ plane) are considered; therefore, for clarity of the exposition, only the two-dimensional formulation will be presented in the rest. The filtered continuity equation is

$$\frac{\partial \bar{u}_1}{\partial x_1^*} + \frac{\partial \bar{u}_2}{\partial x_2^*} - \frac{\partial \bar{u}_1}{\partial x_2^*}\frac{\partial \bar{\eta}}{\partial x_1^*} - \frac{\partial \beta}{\partial x_2^*} = 0, \tag{15}$$

where

$$\beta = \overline{u_1 \frac{\partial \eta}{\partial x_1^*}} - \bar{u}_1 \frac{\partial \bar{\eta}}{\partial x_1^*}. \tag{16}$$

Similarly, the two-dimensional ($i = 1, 2$) filtered momentum equations are

$$\frac{\partial \bar{u}_i}{\partial t^*} + \bar{u}_j \frac{\partial \bar{u}_i}{\partial x_j^*} - \bar{H}_i + \bar{u}_i \frac{\partial \beta}{\partial x_2^*} = -\frac{\partial \bar{p}}{\partial x_i^*} - \frac{\partial \tau_{ij}}{\partial x_j^*} + \frac{\partial \tau_{i2}^\eta}{\partial x_2^*}, \tag{17}$$

where

$$\bar{H}_i = \bar{u}_1 \frac{\partial \bar{u}_i}{\partial x_2^*} \frac{\partial \bar{\eta}}{\partial x_1^*} + \frac{\partial \bar{u}_i}{\partial x_2^*} \frac{\partial \bar{\eta}}{\partial t^*} + \frac{\partial \bar{p}}{\partial x_2^*} \frac{\partial \bar{\eta}}{\partial x_i^*}, \tag{18}$$

$$\tau_{ij} = \overline{u_i u_j} - \bar{u}_i \bar{u}_j \tag{19}$$

and

$$\tau_{i2}^\eta = \left(\overline{u_i u_1 \frac{\partial \eta}{\partial x_1^*}} - \bar{u}_i \bar{u}_1 \frac{\partial \bar{\eta}}{\partial x_1^*} \right) + \left(\overline{u_i \frac{\partial \eta}{\partial t^*}} - \bar{u}_i \frac{\partial \bar{\eta}}{\partial t^*} \right) + \left(\overline{p \frac{\partial \eta}{\partial x_i^*}} - \bar{p} \frac{\partial \bar{\eta}}{\partial x_i^*} \right). \tag{20}$$

The eddy SGS stress, τ_{ij}, corresponds to the effect of the unresolved velocity scale, while the wave SGS stress, τ_{i2}^η, corresponds to the combined effect of both the unresolved velocity and free-surface elevation scales. Note that, by definition, τ_{ij} is a symmetric tensor, while τ_{ij}^η is not since it has nonzero values only in the gravity direction. Due to their dependence on unresolved scales, both SGS stresses have to be modeled. All other terms of the filtered momentum equations (17) are functions of the resolved velocity and free-surface elevation scales, including $\bar{H}_i$.

The filtered dynamic and kinematic free-surface boundary conditions (at $x_2^* = 0$), respectively, become

$$\bar{p} = \frac{\bar{\eta}}{\mathrm{Fr}^2} \tag{21}$$

$$\bar{u}_2 = \frac{\partial \bar{\eta}}{\partial t^*} + \bar{u}_1 \frac{\partial \bar{\eta}}{\partial x_1^*} + \beta. \tag{22}$$

The SGS stresses, τ_{ij} and τ_{ij}^η, will be modeled according to the models presented in Section 3, while the subgrid term β that appears in Eqs. (15), (17), and (22) is set equal to zero because a priori tests of the flows considered in this paper show this term to be negligible.

Transforming back to the physical domain by using $x_1^* = x_1$ and $x_2^* = x_2 + \bar{\eta}$, the filtered continuity equation becomes

$$\frac{\partial \bar{u}_1}{\partial x_1} + \frac{\partial \bar{u}_2}{\partial x_2} - \frac{\partial \beta}{\partial x_2} = 0 \tag{23}$$

while the two-dimensional filtered momentum equations become

$$\frac{\partial \bar{u}_i}{\partial t} + \bar{u}_j \frac{\partial \bar{u}_i}{\partial x_j} + \bar{u}_i \frac{\partial \beta}{\partial x_2} = -\frac{\partial \bar{p}}{\partial x_i} - \frac{\partial \tau_{ij}}{\partial x_j} + \underbrace{\frac{\partial}{\partial x_2} \left(\tau_{i2}^\eta - \tau_{i1} \frac{\partial \bar{\eta}}{\partial x_1} \right)}. \tag{24}$$

Note that these equations are not directly deduced by filtering the original Eqs. (4) and (5) without the intermediate application of the boundary-fitted transformation. Therefore, for free-surface flows, a consistent filtering requires first the application of a boundary-fitted transformation to include the free-surface effect in the equations of motion. With the most simple boundary-fitted transformation chosen in this paper, the effect of the free-surface elevation introduces the underbraced term of the momentum equations (24). More complex transformations will result in more complex forms of this term, depending possibly on higher derivatives of the free-surface elevation and requiring more complex models than the ones presented in the next section.

3. SGS STRESS MODELS

Since the equations of motion derived in the previous section have to be solved only for the resolved scales ($\bar{u}_i$, $\bar{\eta}$), the SGS stresses (τ_{ij}, τ_{ij}^{η}) should be modeled as functions of the resolved scales.

In LES computations, only the eddy SGS stress, τ_{ij}, is present and can be modeled using eddy-viscosity models [17] according to

$$\tau_{ij} = -2\nu_T \bar{S}_{ij} = -2C^2 \bar{\Delta}^2 |\bar{S}| \bar{S}_{ij}, \tag{25}$$

where C is a model parameter, $\bar{\Delta}$ is the length scale related to the filter width (see below), and $|\bar{S}| = (2\bar{S}_{ij}\bar{S}_{ij})^{1/2}$ is the magnitude of the resolved-scale strain-rate tensor:

$$\bar{S}_{ij} = \frac{1}{2}\left(\frac{\partial \bar{u}_i}{\partial x_j^*} + \frac{\partial \bar{u}_j}{\partial x_i^*}\right). \tag{26}$$

The filter width $\bar{\Delta}$ is defined by

$$\bar{\Delta} = (\bar{\Delta}_1 \bar{\Delta}_2)^{1/2}, \tag{27}$$

where $\bar{\Delta}_i$ is the grid spacing in the ith direction.

In LWS, according to (20), the wave SGS stress, τ_{ij}^{η}, is dominated by triple velocity/velocity/free-surface-elevation correlations of the form

$$\overline{u_i u_1 \frac{\partial \eta}{\partial x_1^*}} - \bar{u}_i \bar{u}_1 \frac{\partial \bar{\eta}}{\partial x_1^*}, \tag{28}$$

which are expected to be high in the region just beneath the breaker face where the turbulence intensity and the free-surface slope are the highest during and after breaking. Therefore, in this paper, τ_{ij}^{η} is also modeled using an eddy-viscosity model and is correlated to a modified resolved-scale strain-rate tensor, which incorporates the free-surface elevation effect in the form

$$\tau_{ij}^{\eta} = -2\nu_{\eta} \overline{S_{ij}^{\eta}} \frac{\partial \bar{\eta}}{\partial x_1^*} = -2C_{\eta}^2 \bar{\Delta}^2 \left|\overline{S_{ij}^{\eta}}\right| \overline{S_{ij}^{\eta}} \frac{\partial \bar{\eta}}{\partial x_1^*}, \tag{29}$$

where C_{η} is a model parameter and the modified large-scale strain-rate tensor is

$$\overline{S_{12}^{\eta}} = \frac{\partial \bar{u}_1}{\partial x_1^*}, \qquad \overline{S_{22}^{\eta}} = \frac{1}{2}\left(\frac{\partial \bar{u}_1}{\partial x_2^*} + \frac{\partial \bar{u}_2}{\partial x_1^*}\right), \qquad \overline{S_{i1}^{\eta}} = 0. \tag{30}$$

Apart from (28), the wave SGS stress is also influenced by the term

$$\overline{u_i \frac{\partial \eta}{\partial t^*}} - \bar{u}_i \frac{\partial \bar{\eta}}{\partial t^*}. \tag{31}$$

Using the kinematic free-surface boundary condition (14), the above term (31) becomes

$$\overline{u_i u_{2_{|x_2^*=0}}} - \bar{u}_i \overline{u_{2_{|x_2^*=0}}} - \overline{u_i u_{1_{|x_2^*=0}} \frac{\partial \eta}{\partial x_1^*}} + \bar{u}_i \overline{u_{1_{|x_2^*=0}}} \frac{\partial \bar{\eta}}{\partial x_1^*} \tag{32}$$

and can be modeled similarly to Eqs. (25) and (29). Only the deviatoric part of the SGS stress tensors in (25) and (29) is substituted in the momentum equations (17) because the isotropic part is absorbed into pressure.

Physically, one can think of the wave SGS stresses as the vertical force applied on the resolved scales by the subgrid wave fluctuations as they fall down the front of the spilling breaker. This force adds a shear component in the x_1 momentum direction and a normal component in the x_2 momentum direction, as shown in Eqs. (17) and (24). It should be clarified, though, that modeling of the SGS stresses does not, by itself, constitute modeling of the breaking process; it must be combined with the contribution of the resolved scales dynamics.

The parameters C and C_η can be either constants, like the Smagorinsky model in LES, or functions of time and/or space, in which case they can be evaluated using, for example, a dynamic eddy-viscosity model [11]. In this paper, as a first step in LWS modeling, only constant parameter values are considered in order to demonstrate that an eddy-viscosity model for the wave SGS stresses (which are unique to LWS) is at least as accurate as an eddy-viscosity model for the eddy SGS stresses (which are common to LWS and LES).

4. NUMERICAL IMPLEMENTATION

The numerical methodology used in this paper employs an operator splitting scheme for the temporal integration of the equations of motion, and spectral methods for the spatial discretizations, with Fourier modes in the streamwise direction, and Chebyshev modes in the vertical direction [5].

All unknown flow variables are represented by

$$f(x_1^*, x_2^*, t^*) = \sum_{|l|<L} \sum_{n=0}^{N} f_{ln}(t^*) \exp\left(2\pi \imath \frac{l x_1^*}{B}\right) T_n\left(\frac{2x_2^*}{D} + 1\right), \tag{33}$$

where $2L$ is the number of Fourier modes in the x_1^* direction over the range $[-B/2, B/2]$, N is the number of Chebyshev modes in the x_2^* direction over $[0, -D]$, and $T_n(s)$ is the Chebyshev polynomial of order n, defined in the $[-1, +1]$ range.

To further simplify the numerical solution of the equations of motion, a flow variable transformation is introduced,

$$\begin{aligned} \bar{u}_1^* &= \bar{u}_1 \\ \bar{u}_2^* &= \bar{u}_2 - \frac{\mathrm{d}\bar{\eta}}{\mathrm{d}t^*} \\ \bar{p}^* &= \bar{p}, \end{aligned} \tag{34}$$

by which the continuity Eq. (15) becomes

$$\frac{\partial \overline{u}_i^*}{\partial x_i^*} = 0, \tag{35}$$

and the filtered momentum Eqs. (17) in rotational form [6] become

$$\frac{\partial \overline{u}_1^*}{\partial t^*} = -\overline{u}_2^* \omega - \frac{\partial \Pi}{\partial x_1^*} + \frac{\partial \overline{p}^*}{\partial x_2^*}\frac{\partial \overline{\eta}}{\partial x_1^*} - \frac{\partial \tau_{1j}}{\partial x_j^*} + \frac{\partial \tau_{12}^{\eta}}{\partial x_2^*} \tag{36}$$

$$\frac{\partial \overline{u}_2^*}{\partial t^*} = -\overline{u}_1^* \omega - \frac{\partial \Pi}{\partial x_2^*} - \frac{\mathrm{d}^2 \overline{\eta}}{\mathrm{d}t^{*2}} - \frac{\partial \tau_{2j}}{\partial x_j^*} + \frac{\partial \tau_{22}^{\eta}}{\partial x_2^*}, \tag{37}$$

where $\Pi = \overline{p}^* + \frac{1}{2}(\overline{u}_1^*)^2 + \frac{1}{2}(\overline{u}_2^*)^2$ is the dynamic pressure head, ω is the vorticity (a scalar in two-dimensional flows) of the resolved flow field and $\mathrm{d}^2/\mathrm{d}t^{*2}$ is the second-order material derivative.

With this flow variable transformation, the boundary conditions on the free-surface become

$$\overline{p}^* = \frac{\overline{\eta}}{\mathrm{Fr}^2}, \qquad \overline{u}_2^* = 0, \tag{38}$$

while as $x_2^* \to -\infty$,

$$\overline{u}_1^* \to U_\infty, \qquad \overline{u}_2^* \to -\frac{\mathrm{d}\overline{\eta}}{\mathrm{d}t^*}, \qquad \overline{p}^* \to 0, \tag{39}$$

where U_∞ is the free-stream flow velocity. For the numerical implementation, the x_2^* domain is truncated at a sufficient depth, D, so the previous boundary conditions (39) are implemented at $x_2^* = -D$.

The numerical solution of this new form of the momentum equations is carried out using a fractional time step method. At the first stage of each time step, the nonpressure, nonlinear terms of Eqs. (36) and (37) are treated explicitly,

$$\frac{(\hat{u}_1)^{n+1} - (\overline{u}_1^*)^n}{\Delta t} = \left(-\overline{u}_2^* \omega - \frac{\partial \tau_{1j}}{\partial x_j^*} + \frac{\partial \tau_{12}^{\eta}}{\partial x_2^*}\right)^n \tag{40}$$

$$\frac{(\hat{u}_2)^{n+1} - (\overline{u}_2^*)^n}{\Delta t} = \left(-\overline{u}_1^* \omega - \frac{\mathrm{d}^2 \overline{\eta}}{\mathrm{d}t^{*2}} - \frac{\partial \tau_{2i}}{\partial x_j^*} + \frac{\partial \tau_{22}^{\eta}}{\partial x_2^*}\right)^n, \tag{41}$$

where the superscript, n, denotes the current time step number, $\hat{u}_i$ are the first intermediate velocities, and Δt is the time step.

At the second stage of each time step, the pressure terms of the momentum Eqs. (36) and (37) are treated implicitly using a predictor–corrector iteration method which iterates on the pressure head, Π. The second set of intermediate velocities is defined,

$$(\hat{\hat{u}}_1)_m^{n+1} - (\hat{u}_1)^{n+1} = \Delta t \left(\frac{\partial \overline{\eta}}{\partial x_1^*}\right)^n \left(\frac{\partial \overline{p}^*}{\partial x_2^*}\right)_{m-1}^{n+1} \tag{42}$$

$$(\hat{\hat{u}}_2)_m^{n+1} - (\hat{u}_2)^{n+1} = 0, \tag{43}$$

where the subscript, m, denotes the current predictor–corrector iteration number. For the special case of $m = 1$, the pressure value from the preceding time step is used in Eq. (42).

At the third and final stage of each time step, the velocity field at the next time step is obtained by

$$\frac{(\bar{u}_1^*)^{n+1} - (\hat{\hat{u}}_1)_m^{n+1}}{\Delta t} = -\left(\frac{\partial \Pi}{\partial x_1^*}\right)_m^{n+1} \tag{44}$$

$$\frac{(\bar{u}_2^*)^{n+1} - (\hat{\hat{u}}_2)_m^{n+1}}{\Delta t} = -\left(\frac{\partial \Pi}{\partial x_2^*}\right)_m^{n+1}. \tag{45}$$

By combining Eqs. (44) and (45), and applying the continuity equation, $(\partial \bar{u}_i^*/\partial x_i^*)^{n+1} = 0$, a Poisson equation is obtained for Π,

$$\left(\frac{\partial^2 \Pi}{\partial x_1^{*2}} + \frac{\partial^2 \Pi}{\partial x_1^{*2}}\right)_m^{n+1} = \frac{1}{\Delta t}\left(\frac{\partial \hat{\hat{u}}_i}{\partial x_i^*}\right)_m^{n+1}, \tag{46}$$

which is solved using the tau method to account for the pressure head boundary conditions. These conditions are the free-surface boundary condition,

$$\Pi_m^{n+1} = \left(\frac{\bar{\eta}}{\mathrm{Fr}^2} + \frac{1}{2}(\bar{u}_1^*)^2\right)^n, \tag{47}$$

obtained from Eqs. (38), and the boundary condition at $x_2^* = -D$,

$$\left(\frac{\partial \Pi}{\partial x_2^*}\right)_m^{n+1} = 0, \tag{48}$$

obtained from Eqs. (37) and (39).

A new estimate of the pressure term $\partial \bar{p}^*/\partial x_2^*$ is found from the current estimate of the pressure head

$$\left(\frac{\partial \bar{p}^*}{\partial x_2^*}\right)_m^{n+1} = \left(\frac{\partial \Pi}{\partial x_2^*}\right)_m^{n+1} - \left(\bar{u}_1^* \frac{\partial \bar{u}_1^*}{\partial x_2^*} + \bar{u}_2^* \frac{\partial \bar{u}_2^*}{\partial x_2^*}\right)^n, \tag{49}$$

which in turn yields a new estimate for the second intermediate velocities, $\hat{\hat{u}}_i$, according to (42). Then, a new value for Π_m^{n+1} is computed using (46). The error for each corrector–predictor iteration step is measured as

$$e^{m+1} = \max\left|\Pi_{m+1}^{n+1} - \Pi_m^{n+1}\right|. \tag{50}$$

An estimate of the pressure head is accepted as the final pressure head for a given time step $(n+1)$ when the error measure is below a prescribed threshold, ε. For all numerical simulations presented in this paper, the value $\varepsilon = 10^{-6}$ is used.

The resulting pressure head, Π^{n+1}, is used to determine the velocity, $(\bar{u}_i^*)^{n+1}$, at the next time step using Eqs. (44) and (45). Finally, the boundary condition (39) is applied to solve for the free-surface elevation at the $(n+1)$ time step:

$$\left(\frac{\partial \bar{\eta}}{\partial t^*} + U_\infty \frac{\partial \bar{\eta}}{\partial x_1^*}\right)^{n+1} = -\left(\bar{u}_{2_{|x_2^* = -D}}^*\right)^{n+1}. \tag{51}$$

The global time-accuracy of this numerical scheme is $O(\Delta t)$. Although the local error for each stage of the time step is of higher order, the accuracy for each full time step is lowered because the operations involved in the three stages do not commute.

5. A PRIORI TESTS

In this section, a priori testing results are presented where the predicted modeled SGS stresses are compared to the actual SGS stresses for two free-surface flows.

For the flows presented, the results of two-dimensional direct Euler numerical simulations (DENS) are used to compute both the actual SGS stresses, according to Eqs. (19) and (28), and the modeled SGS stresses, according to Eqs. (25) and (29). The numerical methodology for the DENS is the same with the one described in the previous section apart from the fact that the SGS terms are not present. The resolved velocity components, $\bar{u}_1$ and $\bar{u}_2$, and the resolved free-surface elevation, $\bar{\eta}$, are obtained by retaining only a portion of the DENS Fourier modes according to the following sharp Fourier cutoff filter,

$$\bar{G}(k) = \begin{cases} 1 & \text{if } k \le k_{\max} \\ 0 & \text{if } k > k_{\max}, \end{cases} \tag{52}$$

where $k_{\max} = \pi/\Delta_1$ is the highest wavenumber resolved. In wave space, the convolution equation (1) simplifies to $\bar{f}(k,\ x_2^*,\ t^*) = \bar{G}(k)\, f(k,\ x_2^*,\ t^*)$.

For clarity of the a priori comparisons, the eddy and wave SGS stresses are presented after they are averaged and scaled according to the following definitions:

$$\frac{\langle \tau_{ij} \rangle}{\langle T_{ij} \rangle_{\max}} = \frac{\int \tau_{ij} \mathrm{d}x_1^* \mathrm{d}t^*}{\max[\int T_{ij} \mathrm{d}x_1^* \mathrm{d}t^*]_{x_2^*}} \tag{53}$$

$$\frac{\langle \tau_{ij}^{\eta} \rangle}{\langle T_{ij} \rangle_{\max}} = \frac{\int \tau_{ij}^{\eta} \mathrm{d}x_1^* \mathrm{d}t^*}{\max[\int T_{ij} \mathrm{d}x_1^* \mathrm{d}t^*]_{x_2^*}}, \tag{54}$$

where

$$T_{ij} = (u_i - \langle u_i \rangle)(u_j - \langle u_j \rangle) \tag{55}$$

are the Reynolds stresses of the flow. In Eqs. (53) and (54), the scaling factor is the maximum value over depth (x_2^* direction) of the appropriate averaged Reynolds stress. All SGS stresses are scaled with respect to the Reynolds stresses of the flow in order to reveal their size, and therefore significance, with respect to the large-scale dynamics of the flow. In this paper, the smallest resolved scale was chosen so that the SGS stresses are always of order not larger than about 10% of the corresponding Reynolds stresses.

5.1. *Gravity Wave and Surface Wake Interaction*

The first flow to be considered involves the interaction between a plane gravity wave and a two-dimensional parallel wake flow.

Experiments [15] have investigated the free-surface breaking conditions of such a wave/shear interaction using the following configuration in a towing tank: a submerged moving hydrofoil is used to generate a steady gravity wave, while a thin Mylar sheet is dragged

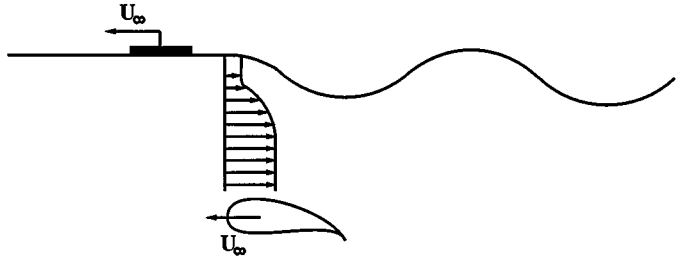

FIG. 2. Experimental setup for gravity-wave/surface-wake interaction. A submerged hydrofoil with speed U_∞ generates a steady gravity wave, while a thin Mylar sheet dragged along the surface with identical speed U_∞ generates the surface wake. The wake velocity profile is presented from a frame of reference moving with velocity U_∞.

along the surface to generate the surface wake (see Fig. 2). Both the submerged hydrofoil and the sheet move with speed $U_\infty = 80$ cm/s. This flow was also studied by DENS [15] using, initially, a two-dimensional parallel shear flow to model the sheet wake, and a plane gravity wave to model the hydrofoil wave. The DENS results are used for the a priori tests in this paper.

The initial velocity profile of the parallel shear flow corresponds to the mean velocity profile measured in the wake of the Mylar sheet at a streamwise distance corresponding to the location where the free surface crosses the mean water level just upstream of the wave crest. This profile, in the frame of reference moving with velocity U_∞, is fitted by the dimensionless expression,

$$u_1(x_2) = 1 - q(1 - \tanh^2(\sigma x_2)), \qquad q = 1 - \frac{U_o}{U_\infty}, \tag{56}$$

where U_∞ is the free-stream velocity (equal to the hydrofoil and sheet speeds), U_o is the free-surface velocity and σ is a fitting parameter. The parameters considered in this study are $q = 0.3$ and $\sigma = 0.88137$, and the corresponding velocity profile is displayed in Fig. 3. Note that the characteristic length scale, b, of this flow is the half-width of the velocity profile (56) corresponding to the dimensionless depth $x_2 = -1$, where $u_1 = (U_\infty + U_o)/2$.

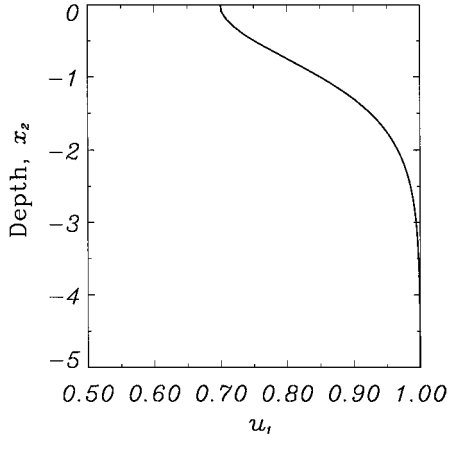

FIG. 3. Dimensionless velocity profile for shear flow (56) with $q = 0.3$ and $\sigma = 0.88137$.

The plane gravity wave, which defines the initial free-surface elevation, η, is represented by a second-order Stokes wave with dimensional wavelength $\lambda = 2\pi U_\infty^2/g$, according to linear theory, and dimensionless amplitude α

$$\eta(t=0) = \alpha\cos(kx_1) + \frac{1}{2}k\alpha^2\cos(2kx_1), \tag{57}$$

where the dimensionless wavenumber, k, of the gravity wave is related to the Froude number of the flow according to

$$k = \frac{2\pi b}{\lambda} = \frac{gb}{U_\infty^2} = \frac{1}{\mathrm{Fr}^2}. \tag{58}$$

For the first a priori tests presented, the case with $\mathrm{Fr} = 3.6$ and amplitude $\alpha = 2.33$ ($k\alpha \approx 0.18$) is considered, which experiments show corresponds to a weak breaking wave with steepness (waveheight/wavelength) very close to the incipient breaking condition [15]. An incipient breaking wave is defined as a nonbreaking wave for which even a slight increase in steepness will cause breaking. The DENS results indicate that the wave begins to break at about $t = 70$. The amplitude of the wave at this time corresponds to the experimentally measured wave amplitude at its breaking point [15]. For the DENS, a time step of 0.00025 was used, with 64 Fourier modes in the x_1^* direction ($B = 2\pi\mathrm{Fr}^2 = 81.43$) and 64 Chebyshev modes in the x_2^* direction ($D = 40$).

In order to define the filtered velocity components, $\bar{u}_1$ and $\bar{u}_2$, only the first 24 low-order Fourier modes and all 64 Chebyshev modes are retained. The actual eddy and wave SGS stresses are computed according to Eqs. (19) and (28), and scaled as described in Eqs. (53) and (54). The modeled eddy and wave SGS stresses are computed according to Eqs. (25) and (29) and similarly scaled.

The scaled mean of the actual and modeled eddy SGS stresses, τ_{ij}, and of the actual and modeled wave SGS stresses, τ_{ij}^η, are displayed in Fig. 4. The eddy SGS component τ_{22} is not plotted since $\tau_{22} = -\tau_{11}$. The solid lines indicate the scaled mean of the actual SGS stresses, while the symbols indicate the scaled mean of the modeled SGS stresses where the values of C and C_η are provided by the best fit in the least squares sense [12]. This constant of best fit is allowed to vary between stress components. In these figures, it is shown that the gross features of the actual SGS stresses are captured by the a priori modeled SGS stresses for an appropriate eddy-viscosity constant. This is especially true in the case of the shear stresses (τ_{12} and τ_{12}^η), which are at least one order of magnitude more significant than the normal stresses (τ_{11} and τ_{22}^η). This relative size difference between the various stress components indicates that the shear SGS stresses have a larger impact on this flow. Different models are used for τ_{ij} and τ_{ij}^η; therefore, it is appropriate to have different constants for each model; that is, $C \neq C_\eta$. However, the eddy-viscosity constant can not vary between the components of τ_{ij} and τ_{ij}^η. In this case, where the shear eddy SGS stresses are more significant than the normal eddy SGS stresses, it is more important that the constant C be appropriate for τ_{12}, as long as C does not significantly increase the magnitude of τ_{11} and τ_{22}. This is also the case for the constant C_η when modeling the shear wave SGS stresses.

A second set of a priori tests was performed on the same flow with a different wave amplitude, $\alpha = 2.59$ ($k\alpha \approx 0.20$). This is a flow where the experiments by Miller *et al.* [15] show that wave breaking is strong. The DENS computational parameters are the same as in the previous example. Figure 5 displays the scaled mean SGS stresses for this case,

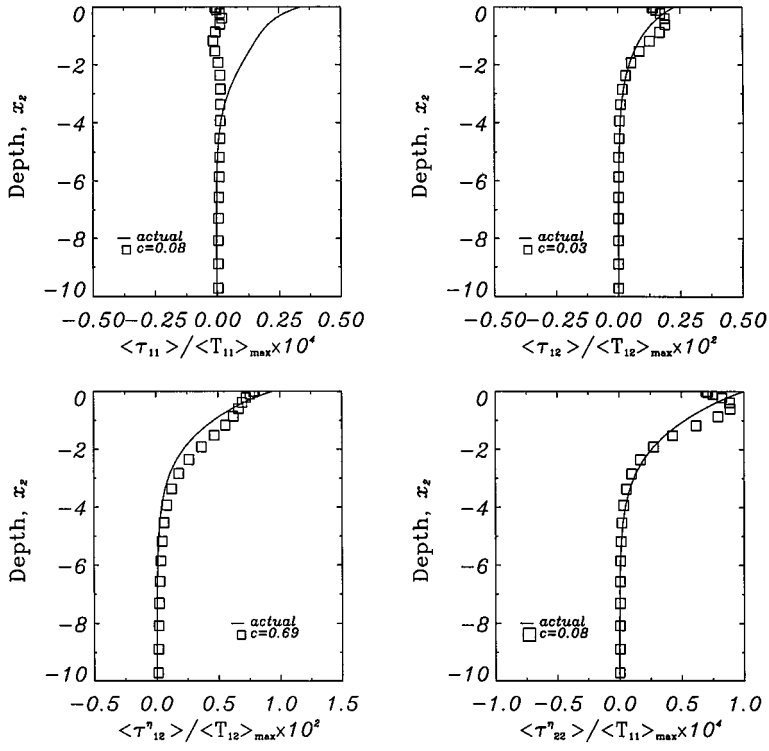

FIG. 4. A priori tests comparing actual to model scaled mean SGS stresses for the gravity-wave/surface-wake interaction, with $\alpha = 2.33$. Values of C and C_η are best fit in least squares sense. For this case, $\langle T_{11}\rangle_{\max} = 1.3 \times 10^{-2}$ and $\langle T_{12}\rangle_{\max} = 8.6 \times 10^{-4}$.

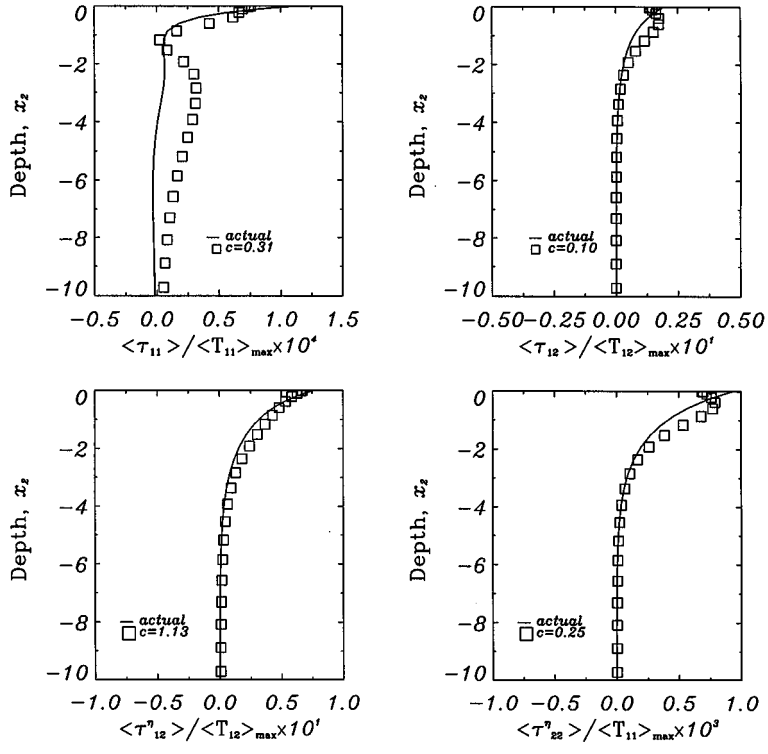

FIG. 5. A priori tests comparing actual to model scaled mean SGS stresses for the gravity-wave/surface-wake interaction, with $\alpha = 2.59$. Values of C and C_η are best fit in least squares sense. For this case, $\langle T_{11}\rangle_{\max} = 1.8 \times 10^{-2}$ and $\langle T_{12}\rangle_{\max} = 1.1 \times 10^{-3}$.

where the values of C and C_η vary for each stress and are provided by the least squares fit to the actual stress. The a priori model captures well all the stresses, regardless of their comparative size.

When observing the values for C and C_η provided by the least squares fit for both cases presented ($\alpha = 2.59$ and $\alpha = 2.33$), it is interesting to note that the best fit values for the largest eddy SGS stresses of each case, $C = 0.10$ and $C = 0.03$, are of the same order with the traditional Smagorinsky constant value of $C = 0.18$. The best fit values for the largest wave SGS stresses of each case, $C_\eta = 1.13$ and $C_\eta = 0.69$, are one order larger than the Smagorinsky constant. Therefore, both of these a priori test cases indicate that the best fit to the actual SGS stresses is achieved when the constants C and C_η are allowed to have differing values; that is, $C \neq C_\eta$.

5.2. *Shear Layer and Free Surface Interaction*

The second flow addressed is the evolution of a two-dimensional, parallel shear flow with an initially flat free surface. The nonlinear growth of the instability of this shear flow and its free-surface manifestation develop spilling breakers due to an increasingly steep free-surface slope with a small amplitude. This flow has been studied by Dimas and Triantafyllou [6], who show that DENS is unable to continue past the breaking point. No experimental measurements are available for this flow.

The initial dimensionless velocity profile of the shear flow is the same as in (56), with a different value for q, and is displayed in Fig. 6. The parameter values used, $q = 0.9988$ and $\sigma = 0.88137$, correspond to a velocity profile measured in the near-wake of a NACA-0003 hydrofoil in unbounded fluid [14]. The Froude number is $\mathrm{Fr} = 0.5$.

For the DENS, a time step of 0.004 was used, with 64 Fourier modes along the x_1^* direction ($B = 2\pi/k = 15.7$, where $k = 0.4$ is the wavelength of the most unstable wave), and 48 Chebyshev modes in the x_2^* direction ($D = 12$). At time $t = 0$, a small amplitude disturbance is applied to the flow; the linear instability wave associated with this disturbance defines the initial free-surface elevation and wavelength. For the a priori computation of the modeled SGS stresses, only the first 16 low-order Fourier modes are retained to define the filtered velocity components, $\bar{u}_1$ and $\bar{u}_2$, while all 48 Chebyshev modes are retained.

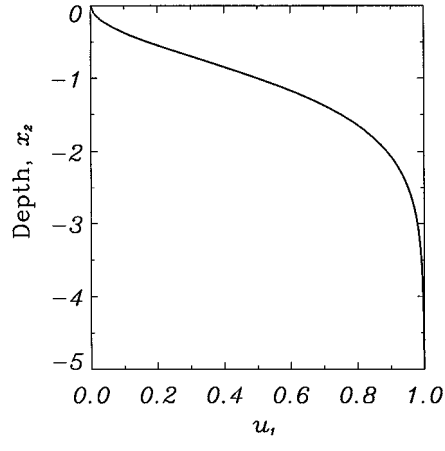

FIG. 6. Dimensionless velocity profile for shear flow (56) with $q = 0.9988$ and $\sigma = 0.88137$.

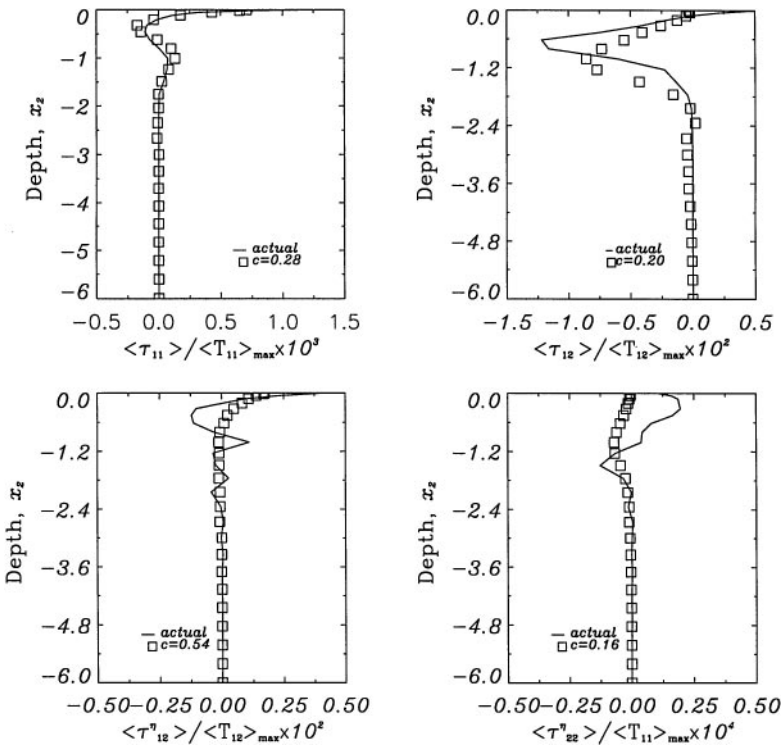

FIG. 7. A priori tests comparing actual to model scaled mean SGS stresses for the interaction of a shear flow and its developing free-surface manifestation. Values of C and C_η are best fit in least squares sense. For this case, $\langle T_{11}\rangle_{\max} = 3.6 \times 10^{-2}$ and $\langle T_{12}\rangle_{\max} = 9.7 \times 10^{-4}$.

The a priori tests are displayed in Fig. 7. All of the eddy SGS stresses are captured well by the model, even though there is a large relative size difference between the shear and normal stress components. The DENS data was insufficient to provide a good measure of the actual wave SGS stresses, but the gross characteristics are captured by the modeled wave SGS stresses. In this flow, as opposed to the results of Section 5.1, the shear eddy SGS stress is one order larger than the shear wave SGS stress, indicating that eddy SGS stresses are more significant than wave SGS stresses with respect to the large scales of the flow. One possible explanation for this is that the wave steepness ($\sim$0.0006) is small, whereas the steepness for the weak breaker of Section 5.1 ($\sim$0.06) is much higher. Since the model captures well the more significant eddy SGS stresses in this case, it is a good indication that the constant eddy-viscosity model employed for these stresses is appropriate. Furthermore, an LWS implementation of this flow [4] was successful in avoiding the DENS problems and continue the simulation past the breaking point. These results are not presented here in order to avoid repetition.

6. LWS OF SPILLING BREAKERS

In this section, the results of LWS and LES implementations for the interaction of a gravity wave and a surface wake are presented. The LWS implementation models both the eddy and wave SGS stresses, τ_{ij} and τ^{η}_{ij}, while the LES implementation incorporates

a model only for the eddy SGS stress, τ_{ij}, and neglects the wave SGS stress, τ_{ij}^{η}. The flow domain, initial velocity profile, and initial free-surface elevation are as described in Section 5.1 and shown in Figs. 2 and 3. The spatial discretization for all cases was carried out as described in Section 4, Eq. (33), with 24 Fourier modes in the x_1 direction and 64 Chebyshev modes in the x_2 direction. Apart from any LWS physical modeling advantages, the lower number of modes used for the spatial discretization in the x_1 direction offers a considerable computational time savings over corresponding DENS implementations.

The LWS and LES are implemented with $\alpha = 2.33$, where α is the amplitude of the gravity wave in (57), which corresponds to the weak breaking wave considered in Section 5.1. Several combinations of C and C_η values are considered in order to examine their effect on the large scale dynamics of the flow. An additional LWS is implemented for the case with $\alpha = 2.59$, which corresponds to the strong breaking wave of Section 5.1. All LWS and LES implementations presented here were successful in simulating the two-dimensional free-surface shear flow beyond the formation of breaking waves but with differing large-scale flow features. The results presented in this section will provide insight to the long-term applicability of LWS in terms of extension to more general three-dimensional free-surface flows.

6.1. *A Posteriori Tests*

For the case with $\alpha = 2.33$, a posteriori tests are carried out in which the modeled eddy and wave SGS stresses output from the LWS are compared to the actual and the a priori predicted SGS stresses, which are both computed from the DENS results. All SGS stresses (actual, a priori and a posteriori) are averaged and scaled according to Eqs. (53) and (54).

The a posteriori comparisons are carried out for two LWS runs: $C = 0.03$, $C_\eta = 0.69$; and $C = C_\eta = 0.22$. The first set of constants corresponds to the a priori best fit for each stress tensor, while the second set corresponds to the a priori best fit under the condition that the two constants are equal. The latter set is considered in order to enforce our a priori conclusion that best results are achieved, in general, when the two constants are not equal. The results for the more significant shear SGS stresses are shown in Figs. 8 and 9,

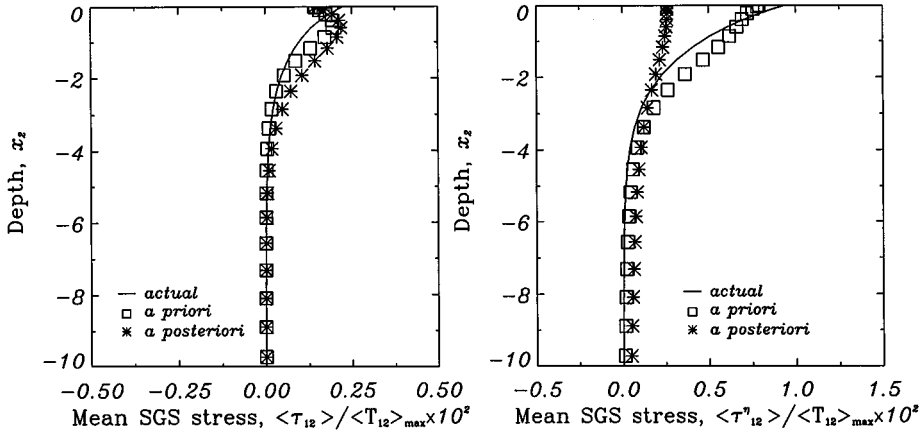

FIG. 8. A posteriori comparison tests of scaled mean SGS stresses for the gravity-wave/surface-wake interaction ($\alpha = 2.33$); modeled stresses are results from LWS implementation with $C = 0.03$ and $C_\eta = 0.69$.

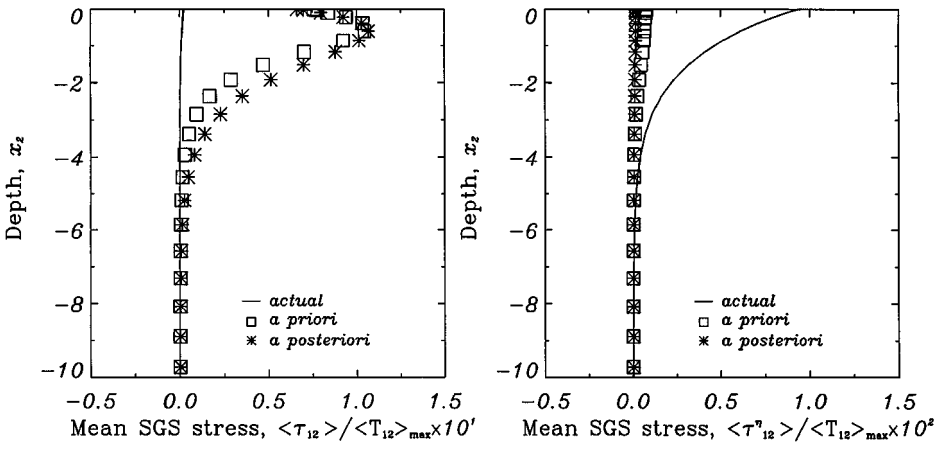

FIG. 9. A posteriori comparison tests of scaled mean SGS stresses for the gravity-wave/surface-wake interaction ($\alpha = 2.33$); modeled stresses are results from LWS implementation with $C = C_\eta = 0.22$.

respectively. The agreement between a priori and a posteriori scaled mean SGS stresses is good, showing that the a priori tests have provided a good means for estimating the values of C and C_η. The first set of constants, though, presents a better agreement between the actual and the a posteriori SGS stresses than the second set.

In terms of the first set of constants ($C = 0.03$, $C_\eta = 0.69$), the a posteriori shear eddy SGS stress, τ_{12}, agrees very well with its corresponding actual stress, indicating that a constant eddy-viscosity model is appropriate for this term. On the other hand, the a posteriori shear wave SGS stress, τ^{η}_{12}, does not show as good an agreement with the actual. This lack of agreement indicates that a dynamic eddy-viscosity model may be more appropriate for modeling τ^{η}_{ij} in this case.

Another set of a posteriori tests are carried out for the case with $\alpha = 2.59$. This LWS implementation was carried out with $C = 0.10$ and $C_\eta = 1.13$, constants which correspond to the a priori best fit for each stress tensor. The results, displayed in Fig. 10, show good

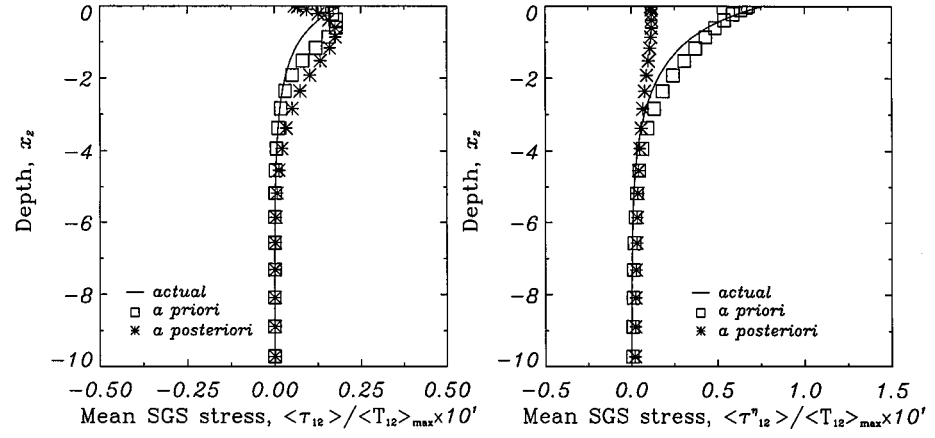

FIG. 10. A posteriori comparison tests of scaled mean SGS stresses for the gravity-wave/surface-wake interaction ($\alpha = 2.59$); modeled stresses are results from LWS implementation with $C = 0.10$ and $C_\eta = 1.13$.

agreement between the a posteriori shear eddy SGS stress (τ_{12}) and the corresponding actual stress. Once again, the agreement is not as good for the shear wave SGS stress, τ_{12}^{η}.

6.2. *Flow Characteristics*

To examine the large scale features of the flow, the weak breaker case with $\alpha = 2.33$ is considered first. The evolution of the free-surface elevation from the DENS and the corresponding LWS with $C = 0.03$ and $C_\eta = 0.69$ are shown in Figs. 11 and 12, respectively. In these figures, the free-surface elevations are stacked in time: they are plotted every $\mathrm{d}t = 5$ time units with a shift along the η axis of $\mathrm{d}\eta = 0.5$ per rendering.

The DENS results present a sharp steepening of the free-surface elevation where the wave crest develops a bulge shape on its forward face. This shape is similar to that found in gentle short-wavelength spilling breakers (see [10]). The point of maximum upward curvature at the leading edge of the bulge is called the toe. In the LWS case, with only 24 Fourier modes, this steepening is not resolvable, therefore, only the large wave scales of the free-surface shape are rendered beyond breaking. This result is also evident in the behavior of the minimum and maximum free-surface slope over time: for the LWS, the slope envelope is fairly flat, while for the DENS, the envelope expands substantially after the breaking point ($t \approx 70$). The free-surface steepening and the subsequent bulge formation just before the breaking point are the characteristics which lead to the numerical problems with DENS of spilling breakers presented in the next paragraph. The grid size is insufficiently fine to resolve the sharp free-surface shape at the toe of the bulge. The LWS overcomes the numerical difficulties associated with the DENS of a breaking wave by resolving only the

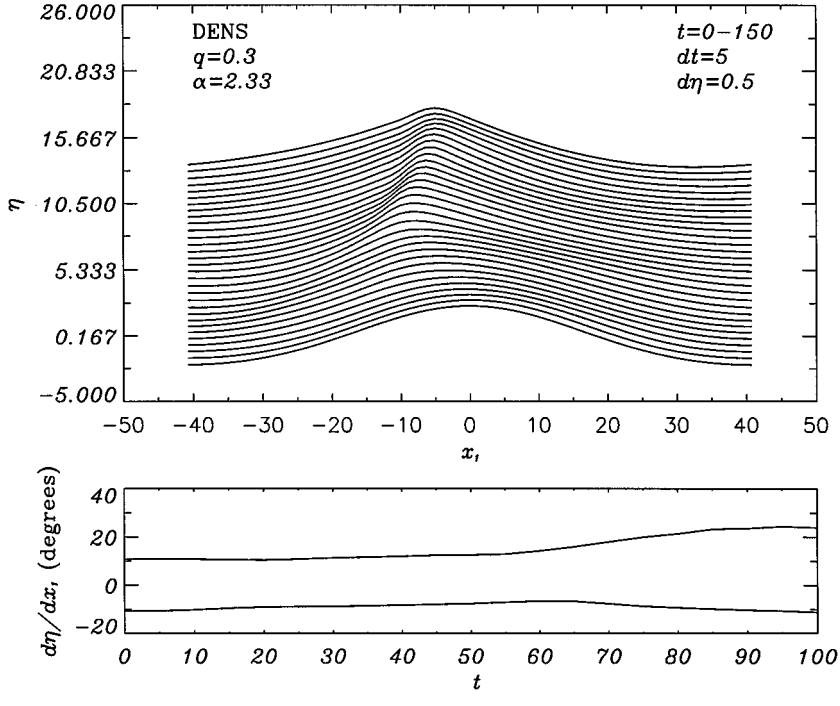

FIG. 11. The evolution of the free-surface elevation and the corresponding minimum and maximum of the free-surface slope from the DENS of the gravity-wave/surface-wake interaction.

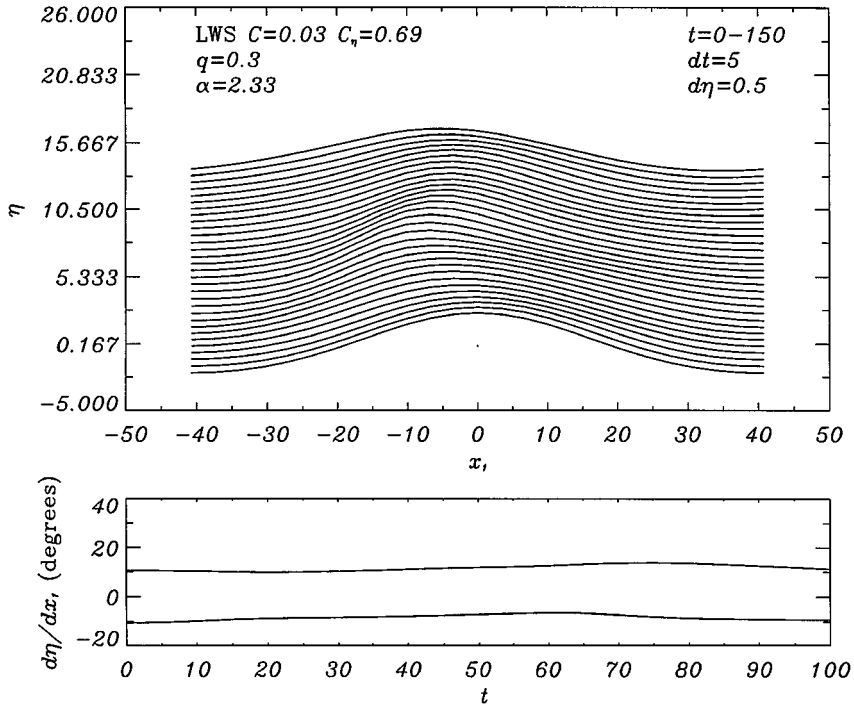

FIG. 12. The evolution of the free-surface elevation and the corresponding minimum and maximum of the free-surface slope from the LWS ($C = 0.03$, $C_\eta = 0.69$) of the gravity-wave/surface-wake interaction.

gross characteristics of the free-surface elevation and not the sharp steepening of the crest nor the postbreaking small fluctuations at the forward face of the breaker. A hint of these postbreaking small fluctuations is evident in Fig. 13, where the difference between the DENS free-surface elevation and the filtered DENS free-surface elevation is plotted. The filtered result is found by a posteriori filtering the free-surface elevation resulting from the

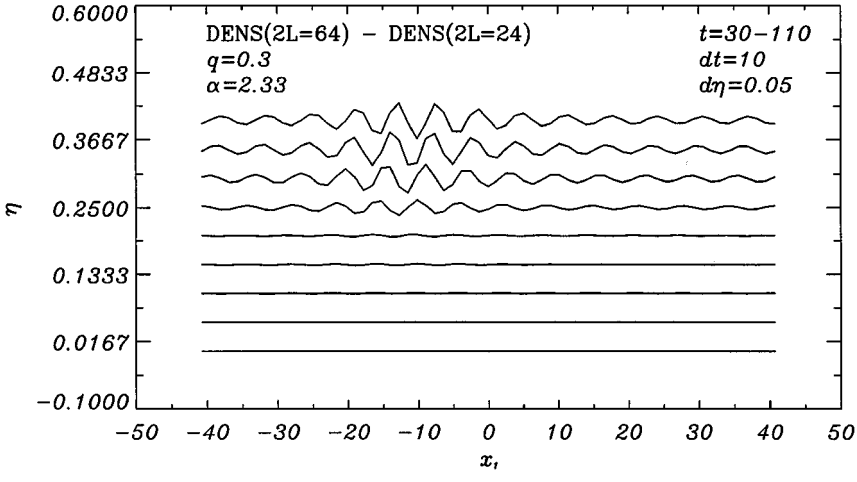

FIG. 13. The difference between the DENS free-surface elevation and the filtered DENS free-surface elevation from $t = 30$ to $t = 110$. The wave breaking point is at $t \approx 70$.

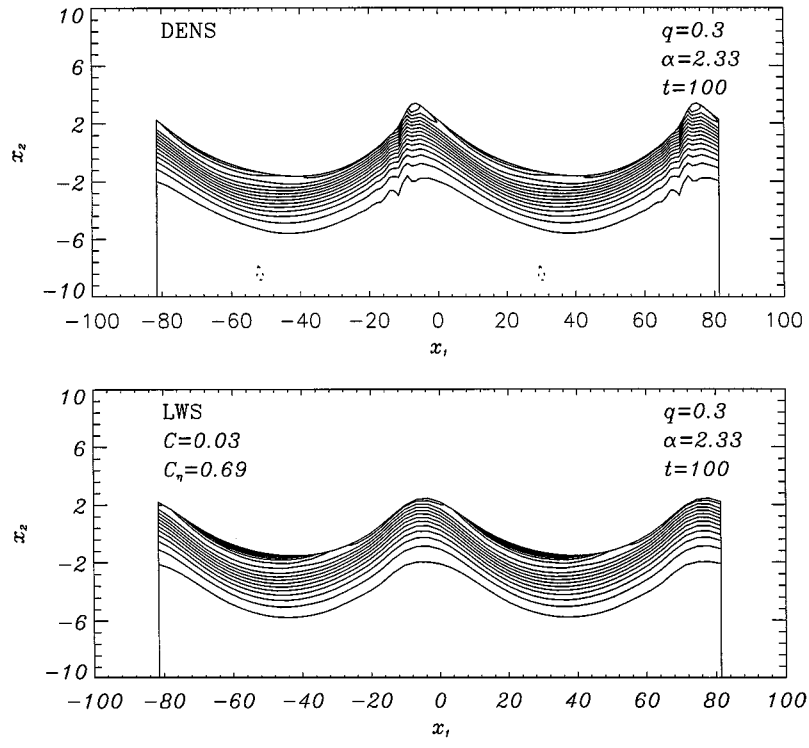

FIG. 14. Vorticity contours from DENS and LWS with $C = 0.03$ and $C_\eta = 0.69$ at time $t = 100$. Solid lines represent negative vorticity, dashed lines represent positive vorticity, and contours are at equal intervals from -0.166 to 0.002, with a spacing of 0.012.

DENS down to 24 Fourier modes. In Fig. 13, the difference between free-surface elevations is plotted every $dt = 10$ time units from $t = 30$ to $t = 110$, with a shift along the η axis of $d\eta = 0.05$. The small fluctuations are most evident right after the breaking point ($t \approx 70$).

In terms of the underlying flow, the DENS results show the development of a numerical instability in the vorticity field close to the free surface at a time which coincides with the incipient wave-breaking event (Fig. 14). It is shown [15] that this instability, displayed as the unphysical lack of smoothness in the vorticity contours, is related to the sharp shape of the free surface at the toe of the bulge that cannot be resolved with any finite number of modes. Obviously, beyond this point the DENS results are not accurate. The vorticity contours from the corresponding LWS run (Fig. 14) are all smooth, and display a weak formation of vortices which are characteristic of the postbreaking behavior of spilling breakers.

In order to study the effect of SGS stresses on the postbreaking flow evolution, several LES and LWS implementations of the weak breaker case are performed. For the effect of eddy SGS stresses, LES computations were carried out for three different eddy-viscosity constant values: the traditional Smagorinsky value of $C = 0.18$, as well as $C = 0.22$ and $C = 0.12$ ($C_\eta \equiv 0$ for all LES). The free-surface elevations and the vorticity contours are very similar for all these runs, indicating that the value of the eddy-viscosity constant between $C = 0.12$ and $C = 0.22$ does not have a strong effect on the dynamic features of the flow. The only difference between these runs is an increasing dissipative effect with increasing values of C due to the diffusive nature of the eddy SGS stress model.

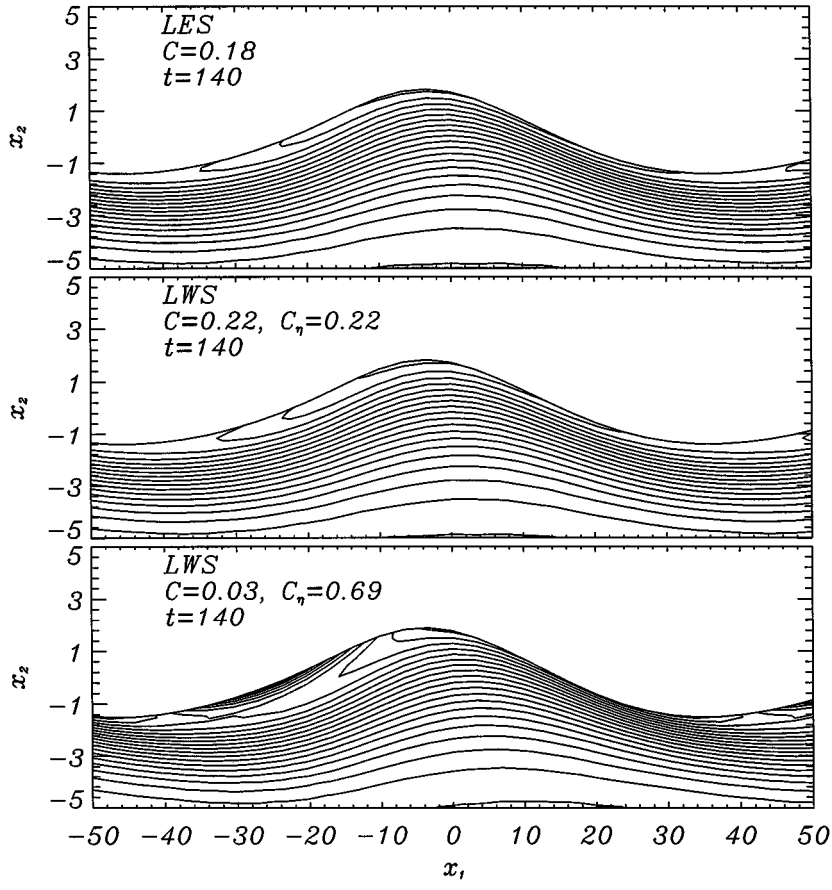

FIG. 15. Vorticity contours for the weak breaker ($\alpha = 2.33$) at time $t = 140$ from LES with $C = 0.18$, LWS with $C = C_\eta = 0.22$, and LWS with $C = 0.03$, $C_\eta = 0.69$. Solid lines represent negative vorticity, dashed lines represent positive vorticity, and contours are at equal intervals from -0.166 to 0.002, with a spacing of 0.007.

For the effect of the wave SGS stresses, first an LWS computation is considered with $C = C_\eta = 0.22$, and is compared to the LES run with $C = 0.22$. Although the results are not identical, there is no significant change in the free-surface elevation nor the vorticity contours from those of the LES computations. Then, the LWS computation with $C = 0.03$ and $C_\eta = 0.69$ is considered. These values correspond to the best fit values for the eddy and wave SGS stresses from the a priori tests in Section 5.1. As with the previous LWS run ($C = C_\eta = 0.22$), there is no significant change in the character of the free-surface elevation. However, there is a significant difference in the vorticity structure well beyond the breaking point.

Figure 15 shows the vorticity contours of a typical LES and the two LWS implementations at $t = 140$, which is well beyond the breaking point. The LWS with the a priori suggested eddy-viscosity constants ($C = 0.03$, $C_\eta = 0.69$) displays the presence of a new vortex at the forward face of the breaker which is qualitatively similar to the characteristic recirculating flow region in the wake of spilling breakers [13]. This structure in the vorticity contours is not present in any of the other results, which displayed only a purely dissipative behavior.

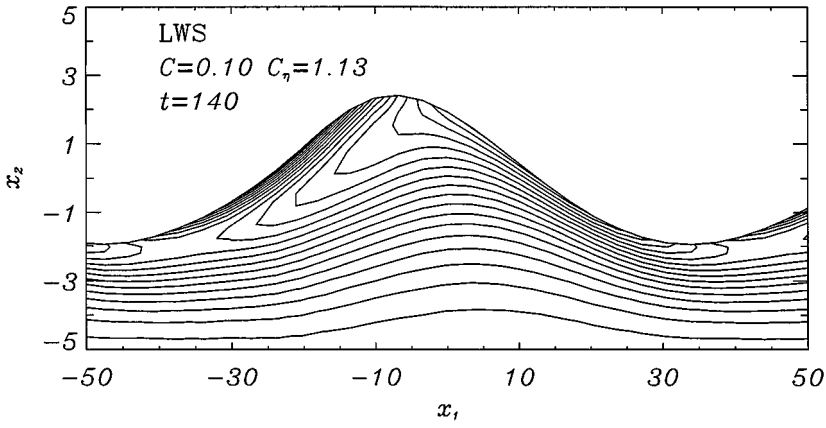

FIG. 16. Vorticity contours for the strong breaker ($\alpha = 2.59$) at time $t = 140$ from LWS with $C = 0.10$, $C_\eta = 1.13$. Solid lines represent negative vorticity, dashed lines represent positive vorticity, and contours are at equal intervals from -0.166 to 0.002, with a spacing of 0.007.

A similar LWS computation is considered for the $\alpha = 2.59$ case, which corresponds to a strong breaking wave. For this case, the values $C = 0.10$ and $C_\eta = 1.13$ are used, which correspond to the best fit values from the appropriate a priori tests in Section 5.1. Figure 16 shows the vorticity contours from this LWS at $t = 140$, where the presence of a new vortex can also be seen. In this case of strong breaking, the DENS computation breaks down soon after the breaking point. Without accurate DENS beyond the breaking point, further quantitative comparisons are needed between the LWS results and future experimental data. In terms of the LWS modeling, the appearance of the breaker vortex in the two LWS results ($\alpha = 2.33,\ C = 0.03,\ C_\eta = 0.69$; and $\alpha = 2.59,\ C = 0.10,\ C_\eta = 1.13$) is probably due to the anisotropic character of τ_{ij}^η.

Finally, the kinetic energy transfer between resolved and subgrid scales is considered for the LWS case with $\alpha = 2.33$ and $C = 0.03,\ C_\eta = 0.69$. The equation for the evolution of the resolved scales kinetic energy can be easily derived from Eq. (17) to be

$$\frac{1}{2}\frac{\partial \bar{u}_i \bar{u}_i}{\partial t^*} + \bar{u}_i \bar{u}_j \frac{\partial \bar{u}_i}{\partial x_j^*} - \bar{u}_i \bar{H}_i = -\bar{u}_i \frac{\partial \bar{p}}{\partial x_i^*} \underbrace{- \bar{u}_i \frac{\partial \tau_{ij}}{\partial x_j^*} + \bar{u}_i \frac{\partial \tau_{i2}^\eta}{\partial x_2^*}}, \tag{59}$$

where the underbraced terms represent the SGS transport, i.e., the total transfer of energy between resolved and subgrid scales.

The instantaneous distribution of the wave SGS transport, $\bar{u}_i \partial \tau_{i2}^\eta / \partial x_2^*$, is displayed in Fig. 17 for time instances well before, during ($t \approx 70$), and well beyond breaking. These plots show that the peak of the wave SGS transport activity: (1) is positive (transfer from subgrid to resolved scales), (2) takes place within a short time just before, during, and just after breaking, and (3) is located in the region underneath the spilling breaker face. All these coincide with the appearance and location of the small-scale fluctuations associated with the breaking process. Although these scales are not resolved, their effect is modeled automatically by LWS. A representative instantaneous distribution of the eddy SGS transport, $-\bar{u}_i \partial \tau_{ij} / \partial x_j^*$, at $t = 60$ is shown in Fig. 18, using the same contour levels as in Fig. 17. It is concluded that during breaking the kinetic energy transfer is dominated by the wave SGS transport.

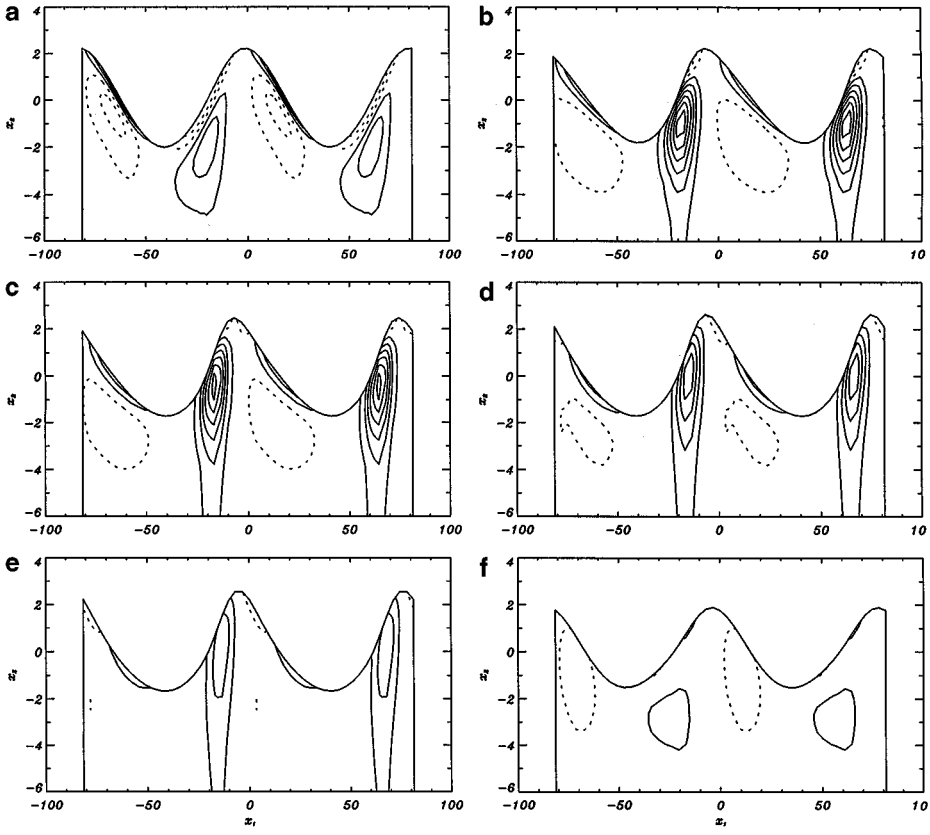

FIG. 17. Contours of the wave SGS transport, $\bar{u}_i \partial \tau_{i2}^{\eta} / \partial x_2^*$, from the LWS of the weak breaker ($\alpha = 2.33$) with $C = 0.03$, $C_\eta = 0.69$. Solid lines represent positive transport, dashed lines represent negative transport, and contours are at equal intervals from -6.0×10^{-6} to 26.0×10^{-6}, with a spacing of 4.0×10^{-6}. (a) $t = 20$, (b) $t = 60$, (c) $t = 70$, (d) $t = 80$, (e) $t = 90$, (f) $t = 140$.

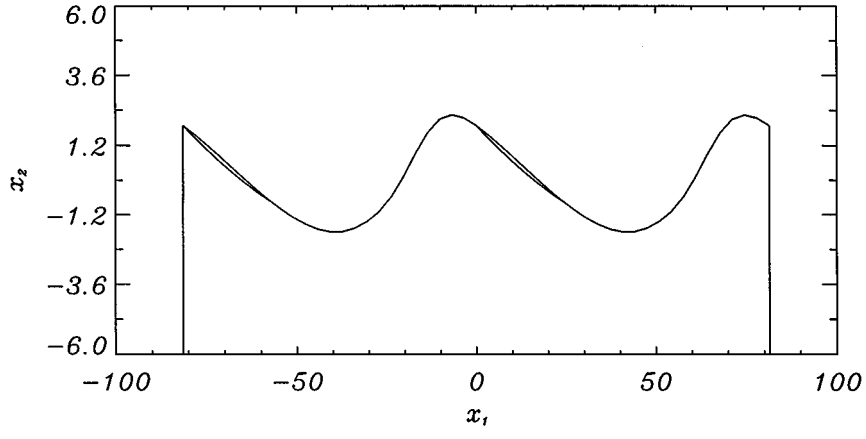

FIG. 18. Contours of the eddy SGS transport, $-\bar{u}_i \partial \tau_{ij} / \partial x_j^*$, at $t = 60$ from the LWS of the weak breaker ($\alpha = 2.33$) with $C = 0.03$, $C_\eta = 0.69$. Solid lines represent positive transport, dashed lines represent negative transport, and contours are at equal intervals from -6.0×10^{-6} to 26.0×10^{-6}, with a spacing of 4.0×10^{-6}.

7. CONCLUSIONS

A method is presented for numerically modeling the evolution of spilling breakers and their shear flow wake beyond breaking where the resolved free-surface shape remains smooth and connected and does not overturn. Filtering and modeling methods similar to LES are applied to the equations of motion, taking into account the free-surface effect by using boundary-fitted coordinates. The resulting LWS filtered equations depend on the resolved scales of velocity, pressure, and free-surface elevation, as well as on eddy and wave SGS stresses which are modeled. Surface tension effects are not considered in this study; therefore, the method presented in this paper is limited to weak spilling breakers. In the future, surface tension effects can be included by filtering the appropriate dynamic free-surface boundary condition and modeling the SGS surface tension effect on the resolved scales.

For the flows considered in this paper, the performed a priori tests show that the structure of the mean eddy and wave SGS stresses is captured well by the constant eddy-viscosity models presented, given the limitation that, as in LES, constant models cannot capture exactly the actual SGS stresses everywhere. These tests conclusively show that a different constant is necessary for the models of the eddy and wave SGS stresses, respectively; i.e., $C \neq C_\eta$. The corresponding a posteriori tests reinforce this conclusion, while also indicating that, although the constant eddy-viscosity model is appropriate for modeling the eddy SGS stresses, a dynamic model may be more appropriate for the wave SGS stresses.

The LWS implementation for the interaction of a gravity wave and a surface wake is successful in simulating this flow past the breaking point where the large-scale features of the flow are in qualitative agreement with experimental observations. In fact, after breaking, a strong vortex develops in the wake of the breaker just beneath the free-surface. It is clearly shown that this effect results from the inclusion of the appropriate wave SGS stresses as the vorticity field for corresponding LES implementations (which neglect the wave SGS stresses) does not demonstrate any vortex formation after breaking.

To improve the LWS models presented in this paper, experimental data should be analyzed in order to provide a possible correlation between the wavelength of the postbreaking free-surface perturbations and the mixing length associated with the eddy-viscosity model for the wave SGS stresses. Furthermore, the simulations should be extended to include three-dimensional effects to better capture turbulence evolution after breaking.

ACKNOWLEDGMENTS

This work was supported in part by the Office of Naval Research.

REFERENCES

1. E. Baba, A new component of viscous resistance, *J. Soc. Naval Archit. Jpn.* **125**, 23 (1969).
2. J. A. Battjes and T. Sakai, Velocity field in a steady breaker, *J. Fluid Mech.* **111**, 421 (1981).
3. S. Chen, D. B. Johnson, P. E. Raad, and D. Fadda, The surface marker and micro cell method, *Int. J. Numer. Methods Fluids* **25**, 749 (1997).
4. A. A. Dimas, Large wave simulations (LWS) of free-surface flows, in *Proceedings, ASME Fluids Engineering Division Summer Meeting* (Vancouver, Canada, 1997), Vol. 3408, pp. 1–6.
5. A. A. Dimas, Free-surface waves generation by a fully submerged wake, *Wave Motion* **27**, 43 (1998).

6. A. A. Dimas and G. S. Triantafyllou, Nonlinear interaction of shear flow with a free-surface, *J. Fluid Mech.* **260**, 211 (1994).
7. J. H. Duncan, An experimental investigation of breaking waves generated by a towed hydrofoil, *Proc. R. Soc. London A* **377**, 331 (1981).
8. J. H. Duncan, The breaking and non-breaking wave resistance of a two-dimensional hydrofoil, *J. Fluid Mech.* **126**, 507 (1983).
9. J. H. Duncan and A. A. Dimas, Surface ripples due to steady breaking waves, *J. Fluid Mech.* **329**, 309 (1996).
10. J. H. Duncan, V. Philomin, M. Behres, and J. Kimmel, The formation of spilling breaking water-waves, *Phys. Fluids* **6**, 2558 (1994).
11. M. Germano, U. Piomelli, P. Moin, and W. H. Cabot, A dynamic subgrid-scale eddy viscosity model, *Phys. Fluids A* **3**, 1760 (1991).
12. P. E. Gill, *Practical Optimization* (Springer-Verlag, New York, 1994).
13. J.-C. Lin and D. Rockwell, Evolution of a quasi-steady breaking wave, *J. Fluid Mech.* **302**, 29 (1996).
14. G. E. Mattingly and W. O. Criminale, The stability of an incompressible two-dimensional wake, *J. Fluid Mech.* **51**, 233 (1972).
15. M. P. Miller, T. Nennstiel, J. H. Duncan, A. A. Dimas, and S. Prostler, Incipient breaking of steady waves in the presence of surface wakes, *J. Fluid Mech.* **383**, 285 (1999).
16. O. M Phillips, Spectral and statistical properties of the equilibrium range in wind-generated gravity waves, *J. Fluid Mech.* **156**, 505 (1985).
17. R. S. Rogallo and P. Moin, Numerical simulation of turbulent flows, *Annu. Rev. Fluid Mech.* **16**, 99 (1984).